J. Fluid Mech. (1992), *vol.* 244, *pp.* 455–476

Nonlinear water waves at a submerged obstacle or bottom topography

By JOHN GRUE

Department of Mathematics, Mechanics Division, University of Oslo,
P.O. Box 1053, Blindern, Norway

(Received 4 April 1991 and in revised form 27 February 1992)

Nonlinear diffraction of low-amplitude gravity waves in deep water due to a slightly submerged obstacle is studied experimentally in a wave channel and theoretically. The obstacle is either a circular cylinder or a rectangular shelf. The incoming waves (with wavelength λ) undergo strong nonlinear deformations at the obstacle when the wave amplitude is finite. An infinite number of superharmonic waves are then introduced to the flow. Their wavelengths far away from the obstacle are $\lambda/4$, $\lambda/9$, $\lambda/16, \ldots,$ due to the dispersion relation being quadratic in the wave frequency. The superharmonic wave amplitudes grow with increasing incoming wave amplitude up to saturation values. They are found to be prominent at the obstacle's lee side and vanishingly small at the weather side. The second- and third-harmonic wave amplitudes are, surprisingly, in several examples found to be comparable to the incoming wave amplitude. Up to 25% of the incoming energy flux may be transferred to the shorter waves. The theoretical model accounts for nonlinearity by the Boussinesq equations in the shallow region above the obstacle, with patching to linearized potential theory in the deep water. The theory explains both qualitatively and quantitatively the trends observed in the experiments up to breaking.

1. Introduction

Low-amplitude ocean waves propagating over shallow reefs, sunken rocks or underwater ridges may, in addition to being diffracted, be broken up into shorter superharmonic free waves due to nonlinear free-surface effects. This is true for swells propagating towards the Norwegian west coast where the bottom topography in many places has several shallow underwater ridges rising from deep water. The generation of the superharmonic waves changes the swell spectrum because a significant part of the incoming wave energy may be transferred to higher frequencies. This phenomenon is observed if one is sailing in a small boat seaward on a day when only swells are propagating towards the shore. Close to land the boat is responding to both longer and shorter waves. By sailing seaward, across the underwater ridges, the shorter waves get weaker and weaker, and in the open sea only the pure swells are observed.

The generation of the free superharmonic waves also occurs at a shallowly submerged marine structure, introducing superharmonic oscillatory forces and contributions to the mean horizontal drift force acting upon the structure. The mean horizontal drift force due to the incoming and scattered waves, which is usually directed along the incoming wave direction, may be reversed when the superharmonic waves generated at the structure's lee side are large.

In the present contribution we study simplified examples of this phenomenon

experimentally in a wave channel and theoretically. Incoming waves with low amplitude propagating in water with great depth are diffracted by a submerged body or a bottom topography which is close to the free surface. The body is a horizontal circular cylinder and the bottom topography is a rectangular shelf. Both geometries have axes parallel to the crests of the incoming waves. The presence of the obstacle introduces locally a shallow fluid depth which leads to significant deformations of the incoming waves as they propagate from the deep water into the shallow region above the obstacle and into the deep water again. The deformations of the waves at the obstacle are linear if the incoming wave amplitude, a, is small compared to the local shallow water depth. Nonlinear effects become prominent at the obstacle when a is finite however. The initially symmetric wave profile then becomes asymmetric and skewed, and the waves may for larger values of a be spilling or plunging. The nonlinear deformations introduce, in addition to oscillations with the same frequency as the incoming wave frequency, ω, a hierarchy of superharmonic oscillations to the flow with frequencies 2ω, 3ω, $4\omega\ldots$, which then generate trains of free waves propagating away from the obstacle. The wavelength of the incoming waves, denoted by λ, is connected to the wave frequency ω, through the dispersion relation

$$\lambda = 2\pi g/\omega^2, \tag{1}$$

assuming that the water depth is greater than λ. By replacing ω by $n\omega$, $n = 2,3,4,\ldots$, in (1) we obtain the wavelengths of the free superharmonic waves as $\lambda/4$, $\lambda/9$, $\lambda/16,\ldots$, which are superposed upon the reflected and transmitted waves with wavelength λ.

The aim of the paper is, by experiments and numerical simulations, to quantify the amplitudes of the superharmonic far-field waves, and to describe their generation in detail. We find that the superharmonic waves are remarkably pronounced at the obstacle's *lee side*. The higher-harmonic wave amplitudes are, for increasing a, growing until saturation values are reached. As we shall see, the second- and third-harmonic free waves may, surprisingly, attain amplitudes which are as large as the first-harmonic transmitted wave amplitude. More specifically, we find that these components may be up to 60% of a. This means that a significant amount of the incoming wave energy flux, up to 25% in the present examples, is transferred to much shorter wave components. The amplitudes of the higher-harmonic waves on the *weather side* of the obstacle are, on the other hand, always very small, even if there is a large first-harmonic reflected wave, or the incoming waves are breaking in front of the submerged obstacle. Thus, the deformations of the incoming waves introduce, practically speaking, changes in the flow only on the lee side of the obstacle.

This problem was studied experimentally and theoretically by Williams (1964) for a horizontal plate situated very close to the free surface. His measurements are basically obtained locally at the plate, with the conclusions that wave components up to the third harmonic are present locally at the plate and in the far field. His results for the far field are, however, complicated to compare with and inconclusive regarding saturation values and breaking limits. We find here, for moderate incoming wave amplitude, qualitatively the same results as Williams, that oscillations up to the third harmonic are introduced to the flow. For larger values of a, we find, however, that very strong nonlinear effects take place locally at the obstacle, which means that the fourth- and higher-harmonic oscillations also are present.

Measurements of second-harmonic free waves generated at a slightly submerged

cylinder are reported by Longuet-Higgins (1977, figure 5) in connection with measurements of negative horizontal drift forces. He finds that the second-harmonic wave amplitude may be as large as approximately 45% of the incoming wave amplitude, and furthermore that it reaches a saturation value, the magnitude of which is not, however, given in his example. Another experimental work, concerning the oscillatory first-, second- and third-harmonic diffraction forces upon a submerged circular cylinder is by Chaplin (1984). He reports measurements of the reflection power due to the circular cylinder, with the conclusion that the first- and higher-harmonic reflected waves always are very small, even if wave breaking occurs at the cylinder. We obtain here the same conclusions as Chaplin regarding the reflection power. Chaplin also mentions that second-harmonic free waves, with prominent amplitude, are generated at the cylinder's lee side without, however, quantifying the amplitude.

The second-harmonic free waves as well as the second-harmonic oscillatory forces may be computed by second order potential theory (Lee 1968; Vada 1987; Friis, Grue & Palm 1991) and for larger values of a by nonlinear simulations, which for a submerged circular cylinder was done recently by Cointe (1989). We compare the measurements of the second-harmonic free wave amplitude with results by the second-order theory, with excellent agreement for small values of the incoming wave amplitude. Cointe's nonlinear simulations for a circular cylinder, originally compared with preliminary experiments by Grue & Granlund (1988), show striking agreement with the experiments, even for larger values of a when saturation is reached.

To provide a simple explanation of the measured results and to illustrate the physical content of the generation mechanism of the superharmonic waves we develop a simplified nonlinear wave diffraction model for the shelf geometry valid for long incoming waves. The model accounts for nonlinearity by the Boussinesq equations in the shallow region above the shelf, with patching at the ends to transient, linearized potential flow applied in the deep water. The patching procedure between the linear and nonlinear flow regimes is very effective, and the model shows good agreement with the experiments both locally at the shelf and in the far field, emphasizing that both nonlinearity and dispersion are important locally at the obstacle, while the linear, dispersive effects are the dominating far away.

The experimental set-up and procedure for the measurements are outlined in §2. We describe in §3 the experimental results for the superharmonic wave amplitudes in the far field. The nonlinear diffraction theory for the shelf is outlined and discussed in §4.

2. Experimental set-up and procedure

The experiments were carried out in a wave channel at the Department of Mathematics at the University of Oslo. The channel is 14.2 m long, 0.47 m broad and is filled with water at a depth which is varied from 0.44 to 0.46 m. At one end the channel is equipped with a wave maker, a vertical rigid plate driven by a hydraulic servo-controlled cylinder, which can perform oscillations under program control. At the other end of the channel there is a 1.5 m long absorbing beach, which reflects less than 10% of the incoming wave amplitude. The wave generation is very accurate and repeatable. The generator is operated such that the incoming waves are pure Stokes waves without second- and higher-harmonic parasitic free waves superposed.

The frequencies of the incoming waves are chosen as either $\omega = 2\pi \times 0.95$ Hz, $2\pi \times 1.05$ Hz or $2\pi \times 1.22$ Hz, with corresponding wavelengths being $\lambda = 1.62$, 1.37 or

1.04 m, respectively. The incoming waves are, practically speaking, deep-water waves, since the wavelengths corresponding to the wave frequencies above for infinite water depth are respectively $\lambda = 1.73$, 1.42 or 1.05 m. The incoming wave amplitude is varied between 2 and 28 mm, which means that the wave slope is smaller than 0.17.

The reflected and transmitted waves are measured for two different circular cylinders and a rectangular shelf, all geometries spanning the whole width of the channel. The smaller cylinder has radius $R = 100$ mm, while the radius of the larger one is $R = 190$ mm. The rectangular shelf has a cross-section 500 mm long and 410 mm high. The uppermost corners of the shelf are well rounded in order to reduce flow separation which may originate there. The geometries are placed with the lee side's furthest extension a distance of 5.7 m from the average position of the wave maker, and with their tops positioned horizontally within a deviation less than 0.2 mm across the width of the channel in order to minimize cross-variations in the flow which can occur at the lee side. The distance h between the uppermost point of the geometries and the mean free surface is varied between 25 and 100 mm.

The surface elevation is recorded by four wave gauges with a resolution of approximately 0.1 mm. The gauges are static calibrated. The accuracy of the analog-to-digital recording of the surface elevation is tested by mounting the gauges on a motorized eccentric which forced the gauges to perform a circular path of a given radius with constant angular velocity in calm fluid, to simulate the recording of oscillatory wave motion. Repeated tests with this arrangement revealed that the recording of the surface elevation has a relative accuracy always better than 5%.

The four gauges are arranged couplewise symmetric with respect to and 12 cm off the centreplane of the channel, and with one couple a distance behind the other. This distance is varied between 10 and 30 cm. The arrangement enables recording of the waves reflected by the geometry, the waves reflected by the beach, the higher-harmonic free waves and the forced components of the Stokes waves. Also, transverse variations, which are observed at the geometry's lee side when wave breaking occurs, are recorded by this arrangement.

First a set of runs was made with the gauges at the weather side, to measure the incoming waves and the reflection power of the obstacle. Next the runs were repeated with the gauges at the obstacle's lee side. The gauges at the weather side and the lee side were placed at different distances from the obstacle. Each experiment was running for 2 minutes before the recording was started. The transients were then small. Then recording continued for 1 minute.

We have also made extensive runs continuing for up to 10 minutes, recording the waves at different starting times and at several stations, obtaining the same experimental results. We have not observed slow-time changes in the wave field.

Wave breaking may occur at the geometry when the incoming wave amplitude is large compared to the local water depth. We here denote, as seems to be standard, the breaking wave as a plunger when air bubbles are clearly observed in the fluid. By spilling we mean a breaking process which does not give rise to air bubbles in the fluid. When wave breaking occurs at the geometry, we observe that variations along the wave crests are introduced at the lee side. The measurements reveal, however, that the variations along the crests occur only for the superharmonic waves and not for the first-harmonic component. The latter result is as expected since the cross-variations introduced by the breaking process contain a minor part of the incoming wave energy, introducing a correspondingly small change in the first-harmonic transmitted wave, which contains the dominant part of the transmitted wave

energy. The higher-harmonic wave components originate from the steep wave at the obstacle however, and small cross-variations there are then continued down-wave of the obstacle. In spite of the presence of the cross-variations in the wave field, the time records of the surface elevation at each geometric location show a steady pattern. This suggests that the cross-variations are simply due to the waves propagating down the channel with crests not exactly orthogonal to the channel walls. By averaging across the channel we obtain results for the higher-harmonic wave amplitudes which are almost independent of the distance from the geometry. Cross-variations in a wave channel may also be due to sloshing modes or cross-waves. The sloshing modes are very small in the present examples since the wave frequencies are chosen different from the cut-off frequencies. Cross-waves are characterized by their subharmonic motions. The experiments show no signs of cross-variations oscillating with frequencies $\frac{1}{2}\omega$, ω or $\frac{2}{3}\omega$ however, which suggests that cross-waves are not introduced by the three lowest-harmonic components $(\omega, 2\omega, 3\omega)$.

Nonlinear resonant interaction between the first-, second- and third-harmonic free waves generated is possible since their wave frequencies and wavenumbers are forming closed tetrads. The time records of the surface elevation at each geometric location show, on the other hand, a steady pattern indicating that this interaction is not taking place in the experiments.

2.1. *Wave kinematics*

Let us introduce the positive x-axis in the mean free surface along the channel length directed towards the beach. The surface elevation η_I of the incoming waves with amplitude a, wavenumber K and wave frequency ω, generated by the wave maker, is

$$\eta_I(x,t) = a\cos(Kx-\omega t+\delta)+a_l^{(2)}\cos 2(Kx-\omega t+\delta)+\ldots, \tag{2}$$

where t denotes time and δ is a phase angle. $a_l^{(2)}$ denotes the amplitude of the forced second-harmonic wave component connected to the incoming wave. For given frequency ω and water depth H the wavenumber K is obtained by the dispersion relation

$$\omega^2 = gK\tanh KH. \tag{3}$$

In the examples considered, $\tanh KH \approx 1$, which means that K deviates very little from the value of the deep-water wavenumber given by ω^2/g. The theoretical value of $a_l^{(2)}$ is thus

$$a_l^{(2)} \cong \tfrac{1}{2}a^2K, \tag{4}$$

which agrees with the experimental observations. We assume that the waves reflected from the obstacle are given by

$$\eta_-(x,t) = a_-^{(1)}\cos(Kx+\omega t+\delta_-^{(1)})+\sum_{n>1} a_{l-}^{(n)}\cos n(Kx+\omega t+\delta_-^{(1)}) + \sum_{n>1} a_-^{(n)}\cos(K_n x+n\omega t+\delta_-^{(n)}), \tag{5}$$

where $a_-^{(n)}$, $n = 1,2,\ldots$, denotes the nth-harmonic reflected free wave amplitudes, $a_{l-}^{(n)}$, $n = 2,3,\ldots$, denotes the amplitudes of the forced nth-harmonic wave components connected to $a_-^{(1)}\cos(Kx+\omega t+\delta_-^{(1)})$ and $\delta_-^{(n)}$, $n = 1,2,\ldots$, are phase angles. The wave numbers K_n, $n = 2,3,\ldots$, are given by

$$(n\omega)^2 = gK_n\tanh K_n H, \quad n = 2,3,\ldots. \tag{6}$$

With $\tanh K_n H$ very close to unity, we obtain

$$K_n = n^2\omega^2/g, \quad n = 2, 3, \ldots. \tag{7}$$

At the lee side of the cylinder we assume that the waves are given by

$$\eta_+(x,t) = a_+^{(1)} \cos(Kx - \omega t + \delta_+^{(1)}) + \sum_{n>1} a_{l+}^{(n)} \cos n(Kx - \omega t + \delta_+^{(1)}) + \sum_{n>1} a_+^{(n)} \cos(K_n x - n\omega t + \delta_+^{(n)}), \tag{8}$$

where $a_+^{(n)}, n = 1, 2, \ldots,$ denotes the nth-harmonic transmitted free wave amplitudes, $a_{l+}^{(n)}$, $n = 2, 3, \ldots,$ denotes the amplitudes of the forced nth harmonic wave components connected to the first-harmonic transmitted wave and $\delta_+^{(n)}$, $n = 1, 2, \ldots,$ are phase angles.

The free wave amplitudes, as well as the forced wave amplitudes, are obtained from the time records of the surface elevation $\eta(x,t)$. Introducing the Fourier transform by

$$\hat{\eta}^{(n)}(x) = \frac{\omega}{2\pi} \int_0^{2\pi/\omega} \eta(x,t) \exp(-in\omega t)\, dt, \quad n = 1, 2, \ldots \tag{9}$$

we may obtain the incoming wave amplitude, a, and the amplitude of the wave reflected by the geometry, $a_-^{(1)}$, by measuring $\hat{\eta}^{(1)}$ at two positions x_1 and $x_1 + \Delta x$ at the weather side. We find

$$a = \frac{1}{|\sin(K\Delta x)|} |\hat{\eta}^{(1)}(x_1) - \hat{\eta}^{(1)}(x_1 + \Delta x) \exp(-iK\Delta x)|, \tag{10}$$

$$a_-^{(1)} = \frac{1}{|\sin(K\Delta x)|} |\hat{\eta}^{(1)}(x_1) - \hat{\eta}^{(1)}(x_1 + \Delta x) \exp(iK\Delta x)|. \tag{11}$$

At the lee side we obtain corresponding results for the first-harmonic transmitted wave and the reflection power due to the beach. We always find that the reflection due to the beach is less than 10 %. The reflection by the beach is even smaller for the shorter higher-harmonic wave components, which gives that the higher-harmonic wave amplitudes at the lee side are obtained by

$$a_+^{(n)} = \frac{1}{|\sin(\frac{1}{2}(K_n - nK)\Delta x)|} |\hat{\eta}^{(n)}(x_1) - \hat{\eta}^{(n)}(x_1 + \Delta x) \exp(inK\Delta x)|, \quad n = 2, 3, 4, \ldots, \tag{12}$$

$$a_{l+}^{(n)} = \frac{1}{|\sin(\frac{1}{2}(K_n - nK)\Delta x)|} |\hat{\eta}^{(n)}(x_1) - \hat{\eta}^{(n)}(x_1 + \Delta x) \exp(iK_n\Delta x)|, \quad n = 2, 3, 4, \ldots. \tag{13}$$

The distance Δx between the gauges is varied between 10 and 30 cm. The position x_1 at the weather side is varied between a distance 0.8 and 1.5 m from the geometry. At the lee side the location of the gauges is varied between 2 and 6.5 m from the geometry. The results obtained for the wave amplitudes with this method are almost independent of the values of Δx and x_1.

3. Experimental results

3.1. *The circular cylinders*

Let us then consider the waves at the lee side of the circular cylinders. In figure 1 (*a*, *b*) we display measurements of $a_+^{(1)}$ and $a_+^{(2)}$ for the circular cylinder with radius $R = 100$ mm submerged with a distance $h = 100$ mm between the free surface and its

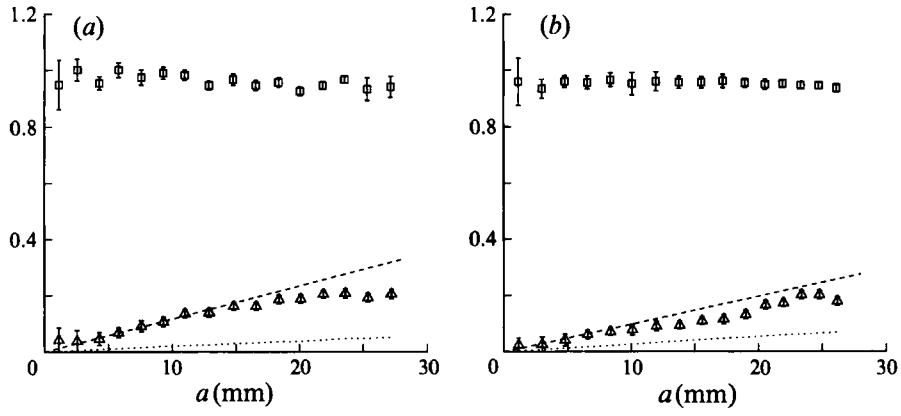

FIGURE 1. Measurements of first- and second-harmonic free wave amplitudes at the lee side of the circular cylinder *vs.* incoming wave amplitude; small cylinder, $R = 100$ mm; $h = 100$ mm: □, $a_+^{(1)}/a$; △, $a_+^{(2)}/a$; ·····, $a_{l+}^{(2)}/a \approx \frac{1}{2}(a_+^{(1)})^2 K/a$; ----, $a_+^{(2)}/a$ obtained by second-order theory (Friis *et al.* 1991). (*a*) $\omega = 2\pi \times 1.05$ Hz, (*b*) $\omega = 2\pi \times 1.22$ Hz.

uppermost point. The scatter obtained by different runs is indicated in the figures. The figures show that $a_+^{(1)}/a$ is always very close to unity. The results for $a_+^{(2)}/a$ exhibit a roughly linear increase with a, which for small and moderate incoming wave amplitude agrees with computations by second-order potential theory (Friis *et al.* 1991). We observe that the second-harmonic wave amplitude $a_+^{(2)}$ is much smaller than $a_+^{(1)}$. $a_+^{(2)}$ is, however, much larger than the forced second-harmonic wave amplitude, $a_{l+}^{(2)}$, which in all examples, within the accuracy of the experiments, agree with the values of $\frac{1}{2}(a_+^{(1)})^2 K$, also shown in the figures. The third- and higher-harmonic waves are very small in these examples.

Next we reduce the distance between the free surface and the uppermost point of the cylinder to $h = 50$ mm. Measurements of $a_+^{(1)}$ and $a_+^{(2)}$ are shown in figure 2(*a*) for the cylinder with $R = 100$ mm and wave frequency $\omega = 2\pi \times 1.05$ Hz, in figure 2(*b*) for $R = 100$ mm and $\omega = 2\pi \times 1.22$ Hz and in figure 2(*c*) for the larger cylinder with $R = 190$ mm and $\omega = 2\pi \times 1.05$ Hz. $a_+^{(3)}, a_+^{(4)}, \ldots$, are again very small.

We observe that the values of $a_+^{(1)}/a$ exhibit a pronounced decay with increasing incoming amplitude, with the largest decay occurring for the largest cylinder. The generation of the large second-harmonic wave must be partly responsible for this decay. In addition, energy loss due to wave breaking and dissipation in the bodies' boundary layer lead to reduced values of $a_+^{(1)}/a$. Since the transfer of energy to the second-harmonic wave and loss of energy due to wave breaking take place with approximately the same strength in all of the three examples, the dissipation seems to be stronger at the larger cylinder, with the larger decay in $a_+^{(1)}/a$, than at the smaller cylinder, with a weaker decay in $a_+^{(1)}/a$.

The values of the second-harmonic free wave amplitude show some interesting features in these examples. We observe that $a_+^{(2)}/a$ is a growing quantity up to a maximum which occurs in the vicinity of the spilling limit, which is also indicated in the figures. Note that the measurements of $a_+^{(2)}$ fit well with the results from second-order potential theory for small incoming wave amplitude. The maximum value of $a_+^{(2)}/a$ is, surprisingly, very close to 0.4 in these examples (figures 2*a* and 2*c*) which means that the magnitude of the second-harmonic free wave amplitude may be comparable to the first-harmonic wave amplitude in these examples. For larger incoming waves $a_+^{(2)}/a$ is a monotonically decaying function. The second-harmonic

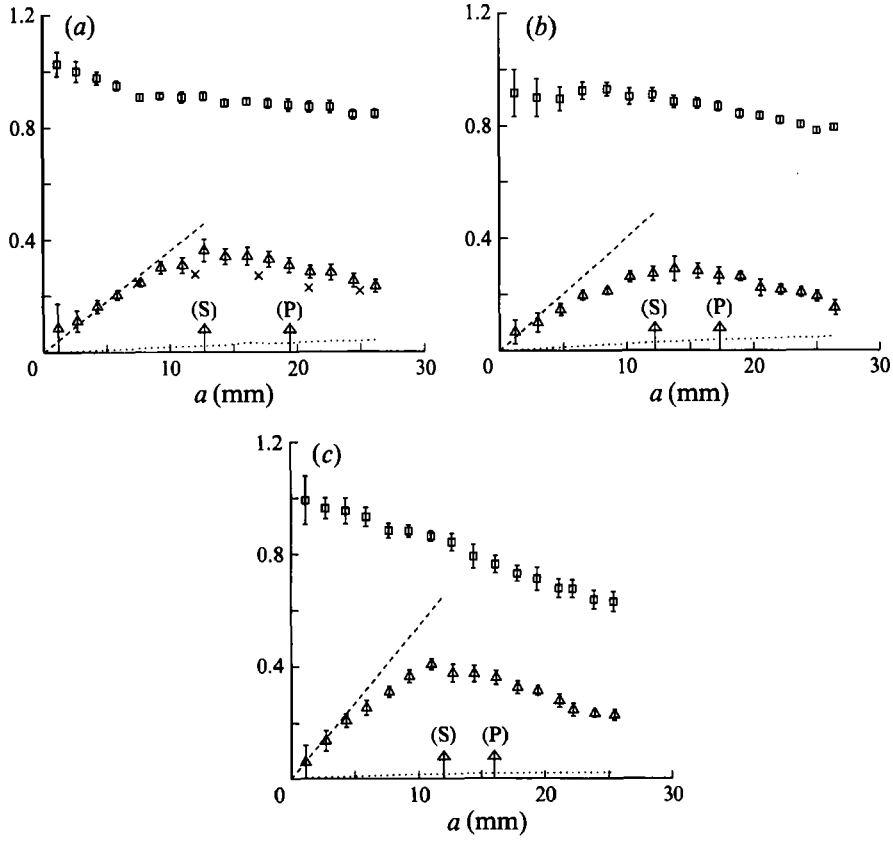

FIGURE 2. As figure 1, but $h = 50$ mm. (*a*) Small cylinder ($R = 100$ mm), $\omega = 2\pi \times 1.05$ Hz: $\times$, $a_+^{(2)}/a$ obtained by nonlinear theory, Cointe (1989, figure 12). (*b*) Small cylinder ($R = 100$ mm), $\omega = 2\pi \times 1.22$ Hz. (*c*) Large cylinder ($R = 190$ mm), $\omega = 2\pi \times 1.05$ Hz. The arrows denote respectively spilling (S) and plunging (P) limits.

free wave amplitude completely dominates the forced second-harmonic wave amplitude in these examples, i.e. $a_+^{(2)} \gg a_{l+}^{(2)}$.

In figure 2(*a*) we have also displayed theoretical results for $a_+^{(2)}$ obtained by Cointe (1989) who exploits potential theory with the exact nonlinear free-surface condition. Cointe's computations, originally compared with Grue & Granlund (1988), are performed for $\omega = 2\pi$ Hz, a slightly smaller frequency than ours. The theoretical results for $a_+^{(2)}$ fit surprisingly well with the present measurements, even when spilling or plunging is observed in the wave flume.

In the next examples, figure 3(*a*, *b*), we consider the smaller cylinder situated very close to the free surface with $h = 25$ mm. The results for $a_+^{(1)}$ and $a_+^{(2)}$ are similar to the cases shown in figure 2(*a*, *b*). The maximum of $a_+^{(2)}/a$ is now occurring for a smaller incoming wave amplitude, $a \approx 5$ mm, with a maximum value being, surprisingly, almost the same as for the deeper submerged circles. Another interesting result is that the experimental values of $a_+^{(2)}$ show excellent agreement with second-order potential theory for very small incoming wave amplitudes, but strongly deviate from this theory for incoming wave amplitudes greater than 5 mm and up to the spilling limit. We would expect second-order theory to be appropriate for obtaining $a_+^{(2)}$ up to the breaking limit. The experimental results indicate, however, that strong

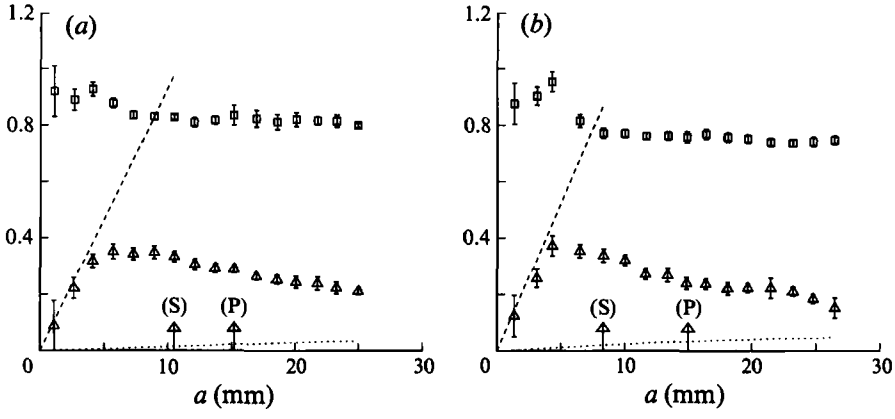

FIGURE 3. As figure 1, for the small cylinder ($R = 100$ mm), but $h = 25$ mm: (*a*) $\omega = 2\pi \times 1.05$ Hz, (*b*) $\omega = 2\pi \times 1.22$ Hz. The arrows denote respectively spilling (S) and plunging (P) limits.

nonlinear effects are contributing to the generation of the second-harmonic waves at the cylinder, which are not included in the second-order theory. As in the former examples, the third- and higher-harmonic waves have very small amplitudes.

One of the striking results for the circular cylinder is that linear potential theory gives a vanishing reflection coefficient (Dean 1948). Very recently, it has been shown by Friis (1990), using the method of Grue & Palm (1985), and by McIver & McIver (1990) that the second-harmonic reflection coefficient is also identically zero. Furthermore, Palm (1991) shows that the dominant part of the nth-harmonic reflection power, $n = 3, 4, \ldots$, vanishes exactly. Our measurements support these theoretical findings. The measured first-harmonic reflection power, $a_-^{(1)}/a$, is always less than 0.05, which is the accuracy of the experiments, even if the waves are breaking at the cylinder. With no first-harmonic reflection, i.e. $a_-^{(1)} \approx 0$, which gives that $a_l^{(2)} \approx 0$, the surface elevation at the weather side of the cylinder is approximately given by

$$\eta(x,t) = a\cos(Kx-\omega t+\delta) + a_l^{(2)}\cos 2(Kx-\omega t+\delta) + a_-^{(2)}\cos(K_2 x+2\omega t+\delta_-^{(2)}) + \text{higher-harmonic components.} \quad (14)$$

It is easy to demonstrate that we may measure $a_-^{(2)}$ using (12) in this case. The measurements show that $a_-^{(2)}$ is much smaller than $a_-^{(1)}$. We also find that $|\hat{\eta}^{(n)}|$, $n = 3, 4, \ldots$, are very small at the weather side of the cylinder. Our experimental results thus indicate that there are no first- and higher-harmonic reflected waves due to a submerged circular cylinder. This result is also found experimentally by Chaplin (1984) who considered circular cylinders with deeper submergence.

3.2. *The rectangular shelf*

In the next examples we consider the higher-harmonic waves generated at the rectangular shelf. The horizontal extent along the wave channel is $2L = 500$ mm and the vertical walls extend down to the channel bottom. The water above the shelf has a constant depth h which is chosen to be either 37.5 or 50 mm. A large part of the incoming wave energy may be reflected by this geometry, depending on the incoming wavelength, the length of the shelf and the local water depth. A major part of the incoming wave energy is, however, transmitted when λ is shorter than about ten times the horizontal extension $2L$, i.e. $\lambda > 20L$.

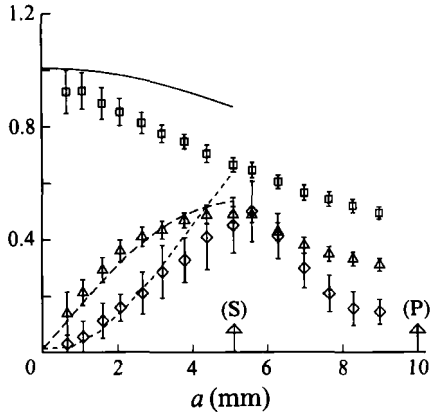

FIGURE 4. First-, second- and third-harmonic free wave amplitudes at the lee side of the rectangular shelf, *vs.* a for $h = 37.5$ mm, $2L = 500$ mm, $\omega = 2\pi \times 0.95$ Hz. Measurements: □, $a_+^{(1)}/a$; △, $a_+^{(2)}/a$; ◇, $a_+^{(3)}/a$. Nonlinear theory: ——, $a_+^{(1)}/a$; – – –, $a_+^{(2)}/a$; ·····, $a_+^{(3)}/a$. The arrows denote respectively spilling (S) and plunging (P) limits.

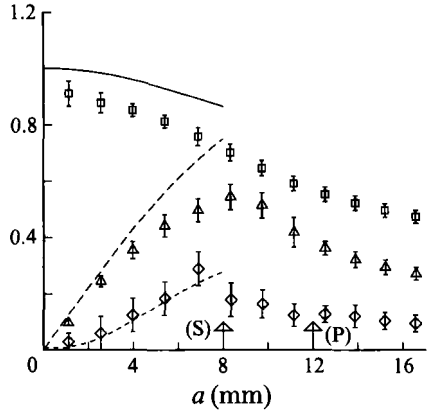

FIGURE 5. As figure 4, but $h = 50$ mm, $\omega = 2\pi \times 1.05$ Hz.

In figure 4 we display measurements of $a_+^{(1)}$, $a_+^{(2)}$ and $a_+^{(3)}$ obtained for $h = 37.5$ mm and $\omega = 2\pi \times 0.95$ Hz. We observe that the generation of the higher-harmonic waves is more powerful in this example than in the previous ones. Interestingly, a pronounced third-harmonic wave is also present. The results for $a_+^{(1)}$ and $a_+^{(2)}$ are very similar to those for the circular cylinders, with the exception that the values of $a_+^{(1)}$ and $a_+^{(2)}$ now are almost of equal magnitude at the spilling limit. Surprisingly, the third-harmonic wave amplitude may be as large as 60% of the incoming wave amplitude and becomes even larger than $a_+^{(2)}$ in the vicinity of the spilling limit. Approximately 25% of the incoming energy flux is transferred to the superharmonic waves at the spilling limit in this case. In figure 5 we display results for another example with the shelf where the parameters are $h = 50$ mm and $\omega = 2\pi \times 1.05$ Hz. In this case the maximal value of $a_+^{(2)}/a$ is approximately 0.6. $a_+^{(3)}/a$ is, however, much smaller in this example than in the former. The fourth- and higher-harmonic waves in these examples have wavelengths shorter than 10 cm. Measurements of such short waves are very complicated since the energy is quickly dissipated.

In both examples with the shelf the measured first-harmonic reflection power is $a^{(1)}/a \approx 0.2$. The amplitudes of the higher-harmonic reflected waves are, however,

smaller than the experimental error. Other examples, not shown here, also show that pronounced higher-harmonic waves are introduced at the lee side of the obstacle, while there are, practically speaking, no such waves at the weather side. This is also the case when there is a large reflected first-harmonic wave.

In figures 4 and 5 we also display theoretical results for $a_+^{(1)}$, $a_+^{(2)}$ and $a_+^{(3)}$. The theory is outlined and discussed in §4. The main idea is to account for nonlinear and dispersive effects in the vicinity of the obstacle with patching to linearized theory describing the flow elsewhere.

3.3. *Saturation*

In all the examples for the circular cylinders and the shelf we find that the generation of the superharmonic wave components takes place with increasing strength for growing wave amplitude up to when breaking occurs at the obstacle. At still higher incoming wave amplitude the transfer of energy to the superharmonic components reduces in power, and we find that the superharmonic wave amplitudes become saturated. The slopes of the superharmonic waves in all the examples are found to be smaller than about 0.1.

3.4. *Dissipation of energy*

We observe in all examples discussed that the dissipation of energy becomes more and more powerful with increasing wave amplitude. The dissipation in the boundary layer at the geometries, being laminar in the present examples, is proportional to $(n\omega)^{\frac{5}{2}}$ times the amplitude of oscillation squared for the nth-harmonic oscillation. Thus, the dissipation becomes more pronounced when the superharmonic oscillations are large, which explains why we observe a stronger dissipation in the examples for the shelf than for the cylinders.

4. Nonlinear theory

The measurements show that the nth-harmonic transmitted wave amplitude is growing proportional to the nth power of the incoming wave amplitude when this is small. For larger a, however, $a_+^{(n)}$ grows slower than a^n. This is true even in the non-breaking regime, see figures 2–5. It is of interest to develop a nonlinear theory which can provide a simple explanation of these features and illustrate the physical content of the problem. Motivated by the flow properties revealed in the experiments, both for the circular cylinders and for the shelf, a simplified theory is developed for the latter geometry. The main idea is to utilize the distinct flow properties of respectively the deep and shallow fluid layers. Characteristic for the experiments is that the incoming waves are of small wave slope and that the waves are long compared to the local depth in the shallow region above the obstacle. This can mathematically be expressed by

$$aK \ll 1, \tag{15}$$

$$Kh \ll 1 \tag{16}$$

and constitutes basic assumptions for the theory. Besides (15) and (16) we assume that the fluid is inviscid and incompressible and the motion irrotational. The theory explains, as we shall see, the experimental results both qualitatively and quantitatively up to when breaking occurs. Linearized theories for the shelf geometry have been studied earlier (see e.g. Newman 1965; Miles 1967; Newman, Sortland & Vinje 1984). The present problem is also related to the problem of linear and nonlinear oscillations occurring in a harbour, a review of which can be found in for example Mei (1989, §5, §11.12).

4.1. *Nonlinear flow in the shallow region*

Coordinates x and y are applied with the x-axis in the mean free surface (as introduced in §2) and the y-axis on the vertical symmetry line of the shelf. The corners of the shelf are then located at $x = \pm L, y = -h$. The water depth h above the shelf is assumed to be small compared to the horizontal extension, $2L$. The depth outside the shelf is assumed infinite. A transient mathematical formulation is adopted, with a wave train incident from $x = -\infty$. The wave train behind the transient front is described by the wavenumber K, frequency $\omega = (gK)^{\frac{1}{2}}$ and amplitude a.

The incoming waves are assumed to be long compared to the local depth in the shallow region above the shelf, which means that the flow there is weakly dispersive. To account for both nonlinear and weakly dispersive effects we apply the nonlinear Boussinesq equations to the flow there, i.e.

$$\frac{\partial \eta}{\partial t} = -\frac{\partial}{\partial x}((h+\eta)\,u), \tag{17}$$

$$\frac{\partial u}{\partial t} + \frac{1}{2}\frac{\partial}{\partial x}u^2 = -\frac{\partial p_{\mathrm{d}}}{\partial x}, \tag{18}$$

where u and p_{d} denote respectively depth-averaged horizontal velocity and dynamical pressure (divided by the fluid density),

$$p_{\mathrm{d}} = g\eta - \frac{h^2}{3}\frac{\partial^2 u}{\partial x\,\partial t}. \tag{19}$$

4.2. *Linear flow outside the shallow region*

The flow at the weather side and the lee side of the shelf, i.e. for $|x| > L$, may according to the previous assumptions be governed by a velocity potential ϕ which satisfies the two-dimensional Laplace equation, $\phi_{xx} + \phi_{yy} = 0$, in the fluid domain. The potential ϕ is subject to the nonlinear free-surface boundary condition. Assuming, however, that the wave slope of the incoming waves is small and that the diffracted waves are also of small wave slope, the free-surface boundary condition may be linearized, i.e. $\phi_{tt} + g\phi_y = 0$ at $y = 0, |x| > L$. At the vertical walls there is no mass flux, i.e. $\phi_x = 0$, at $x = \pm L$, $-\infty < y < -h$. Furthermore, the fluid motion decays to zero, i.e. $|\nabla\phi| \to 0$, as $y \to -\infty$. The initial conditions are that there is no applied pressure at the free surface and no free-surface elevation, i.e. $\phi = \phi_t = 0$, at $t = 0$.

The potential ϕ governing the flow at the weather side ($x < -L$) is appropriately composed of a standing wave potential, ϕ_0, and a velocity potential due to the outflux at $x = -L$, ϕ_{-L}, i.e.

$$\phi = \phi_0 + \phi_{-L}. \tag{20}$$

The standing wave potential corresponding to an incoming and a reflected wave, both with amplitude a and wavenumber $K = \omega^2/g$, is

$$\phi_0(x, y, t) = -2(ag/\omega)\exp(Ky)\cos K(x+L)\sin\omega t. \tag{21}$$

In the simulations a increases monotonically from zero at $t = 0$ to a constant value.

The transient velocity potential ϕ_{-L} may be given by a source distribution over the gap at $x = -L$ with source strength $q_{-L}(y, t)$. By applying the velocity potential due

to one source located at the point $(-L, y')$, satisfying the boundary conditions and initial conditions developed above, ϕ_{-L} is (see Wehausen & Laitone 1960, eqn 13.54)

$$\phi_{-L}(x,y,t) = \frac{1}{2\pi}\int_{-h}^{0} q_{-L}(y',t)\ln\frac{r}{r_1}\mathrm{d}y'$$
$$-\frac{g}{\pi}\int_{-h}^{0}\mathrm{d}y'\int_0^t \mathrm{d}\tau q_{-L}(y',\tau)\int_0^\infty \frac{\mathrm{d}k}{(gk)^{\frac{1}{2}}}\sin[(gk)^{\frac{1}{2}}(t-\tau)]\exp k(y+y')\cos k(x+L), \quad (22)$$

where $r = |x+L+\mathrm{i}(y-y')|$ and $r_1 = |x+L+\mathrm{i}(y+y')|$. The potential ϕ_L governing the flow on the lee side $(x > L)$ may correspondingly be given by a source distribution $q_L(y,t)$ over the gap at $x = L$, i.e.

$$\phi_L(x,y,t) = \frac{1}{2\pi}\int_{-h}^{0} q_L(y',t)\ln\frac{r}{r_1}\mathrm{d}y'$$
$$-\frac{g}{\pi}\int_{-h}^{0}\mathrm{d}y'\int_0^t \mathrm{d}\tau q_L(y',\tau)\int_0^\infty \frac{\mathrm{d}k}{(gk)^{\frac{1}{2}}}\sin[(gk)^{\frac{1}{2}}(t-\tau)]\exp k(y+y')\cos k(x-L), \quad (23)$$

where $r = |x-L+\mathrm{i}(y-y')|$ and $r_1 = |x-L+\mathrm{i}(y+y')|$.

4.3. *Patching*

From (21) and (22) we obtain

$$\frac{\partial}{\partial x}(\phi_0+\phi_{-L}) \to -\tfrac{1}{2}q_{-L}(y,t), \quad x \to -L^- \quad (24)$$

and from (23)

$$\frac{\partial\phi_L}{\partial x} \to \tfrac{1}{2}q_L(y,t), \quad x \to L^+. \quad (25)$$

Introducing the volume flux in the shallow region by

$$Q = u(\eta+h), \quad (26)$$

conservation of mass at the gaps gives

$$\int_{-h}^{0}\frac{\partial\phi(\pm L,y,t)}{\partial x}\mathrm{d}y = Q(\pm L,t). \quad (27)$$

We can show for the linearized case that the vertical variations in $q_{\pm L}$ give contributions to the flow some distance away from the gaps that are asymptotically small in Kh when $Kh \to 0$. This justifies replacing the source distributions at $x = \pm L$ by line sources of constant strength over the gaps provided that $Kh \ll 1$. Applying (24), (25) and (27) we obtain within this approximation that $q_{\pm L}$ are given by

$$q_{-L} = -(2/h)\,Q(-L,t), \quad (28)$$
$$q_L = (2/h)\,Q(L,t). \quad (29)$$

The velocity potentials ϕ_{-L} at $x = -L$, and ϕ_L at $x = L$, then become

$$\phi_{\pm L}(\pm L,y,t) = \pm\frac{Q(\pm L,t)}{\pi h}\int_{-h}^{0}\ln\frac{|y-y'|}{|y+y'|}\mathrm{d}y'$$
$$\mp\frac{2g}{\pi h}\int_0^t \mathrm{d}\tau\, Q(\pm L,\tau)\int_0^\infty \frac{dk}{(gk^3)^{\frac{1}{2}}}\sin[(gk)^{\frac{1}{2}}(t-\tau)](1-\exp(-kh))\exp(ky), \quad (30)$$

where in the last term we have carried out the vertical integration.

The numerical integration of the linearized Boussinesq equations with (30) applied at $x = \pm L$ is compared with the corresponding analytical frequency domain solution. The numerical agreement between the two methods is better than 1 per mille, and indicates the accuracy of the time integration. More refined matching procedures between the flows in the shallow and deep regions have been performed within linearized theory in the frequency domain. We compared our analytical frequency domain solution with the matching procedure exploited by Newman *et al.* (1984), valid for $Kh \ll 1$. The only difference between the two methods appears in one particular factor in the solution, with the following difference for $Kh \ll 1$

$$\ln(4Kh/\pi)+\gamma-1+\pi\mathrm{i} \quad \text{(Newman } et\ al.\text{ 1984, eqn 18)},$$

$$\ln Kh+\gamma-1+\pi\mathrm{i} \quad \text{(present theory)},$$

where $\gamma = 0.5772\ldots$ denotes Euler's constant. The two methods predict the flow characteristics, e.g. the complex reflection and transmission coefficients, with a relative difference which disappears when $Kh \to 0$ and increases monotonically up to about 5% when $kH = \frac{1}{2}$ ($h/2L = O(0.1)$).

The error introduced by the patching between the nonlinear and linear flow regimes can be measured e.g. by invoking the time-averaged energy flux as a function of the horizontal coordinate. This is done in §4.7. We find that there is a net increase across the shelf in the time-averaged energy flux, normalized by the energy flux of the incoming wave, proportional to the incoming wave amplitude when this is finite, see figure 10. This net increase is found to be $\sim 8\%$ at the spilling limit for the example shown in figure 4. This means that the patching has introduced an error $\sim 4\%$ in the free-surface elevation and the fluid velocities, since the dominant part of the energy flux is proportional to the incoming wave amplitude squared. If the incoming wave amplitude is halved, the errors in the free-surface elevation and the velocities due to the patching are consequently $\sim 2\%$.

4.4. *Numerical integration*

Let the domain $|x| \leqslant L$ be subdivided into $N+1$ segments with equal length $\Delta x = 2L/(N+1)$ and let Δt denote a constant time step. Following Pedersen (1991) the Boussinesq equations are integrated by a scheme that is staggered in both time and space, i.e.

$$[\delta_t \eta = -\delta_x\{(1+\overline{\eta}^{xt})\, u\}]_i^{(k+\frac{1}{2})}, \tag{31}$$

$$[\delta_t u + \delta_x T = -\delta_x p_d]_{i+\frac{1}{2}}^{(k)}, \tag{32}$$

where

$$T_{i+\frac{1}{2}}^{(k)} = \tfrac{1}{2}(\overline{u}^x)_{i+\frac{1}{2}}^{(k-\frac{1}{2})}\,(\overline{u}^x)_{i+\frac{1}{2}}^{(k+\frac{1}{2})} \tag{33}$$

and $[\ ]_i^{(k)}$ denotes the value at $x_i = -L + i\Delta x$ at time $t_k = k\Delta t$. The symmetric difference operator, δ_t, and the midpoint average operator, $\overline{(\ )}^t$, of a quantity $f(x,t)$, are introduced by

$$[\delta_t f]_i^{(k)} \equiv \frac{1}{\Delta t}[f(x_i, t_{k+\frac{1}{2}}) - f(x_i, t_{k-\frac{1}{2}})], \tag{34}$$

$$[\overline{f}^t]_i^{(k)} = \tfrac{1}{2}[f(x_i, t_{k+\frac{1}{2}}) + f(x_i, t_{k-\frac{1}{2}})]. \tag{35}$$

The operators δ_x and $\overline{(\ )}^x$ are defined accordingly. Thus, u is obtained at $x_{i+\frac{1}{2}}$, $i = 0, 1, \ldots, N$ at $t_{k+\frac{1}{2}} = (k+\frac{1}{2})\Delta t$, and η at $x_i, i = 1, \ldots, N$ at $t_{k+1} = (k+1)\Delta t$. The overall discretization error of the scheme is $O(\Delta x^2, \Delta t^2)$.

The free-surface elevation, η, and the depth-averaged dynamical pressure (divided by the density), p_d, at $x = \pm L$ are related to the volume flux $u(\eta + h)$ by (20), (21) and (30). This closes the numerical scheme. Evaluation of the memory term in $\partial\phi_{\pm L}/\partial t$ follows Yeung (1982), i.e.

$$\begin{aligned}
&\int_0^{t_k} \mathrm{d}\tau\, Q(\pm L,\tau) \int_0^\infty \frac{\mathrm{d}k}{k} \cos\left[(gk)^{\frac{1}{2}}(t_k-\tau)\right](1-\exp(-kh))\exp(ky) \\
&\quad = \sum_{m=0}^{k-1} Q(\pm L, t_{m+\frac{1}{2}}) \int_{t_m}^{t_{m+1}} \mathrm{d}\tau \int_0^\infty \frac{\mathrm{d}k}{k} \cos\left[(gk)^{\frac{1}{2}}(t_k-\tau)\right](1-\exp(-kh))\exp(ky) \\
&\quad = \sum_{m=0}^{k-1} (Q(\pm L, t_{m+\frac{1}{2}}) - Q(\pm L, t_{m-\frac{1}{2}})) \int_0^\infty \frac{\mathrm{d}k}{(gk^3)^{\frac{1}{2}}} \sin\left[(gk)^{\frac{1}{2}}(t_k-t_m)\right] \\
&\qquad \times (1-\exp(-kh))\exp(ky). \qquad (36)
\end{aligned}$$

We can show that

$$\int_0^\infty \frac{\mathrm{d}k}{(gk^3)^{\frac{1}{2}}} \sin(gk)^{\frac{1}{2}}t\,(1-\exp(ky)) = 2t\mathscr{F}_2[\tfrac{1}{2}t(g/|y|)^{\frac{1}{2}}], \qquad (37)$$

where

$$\mathscr{F}_2(\Omega) = \int_\Omega^\infty \frac{\mathscr{F}(u)}{u^2}\mathrm{d}u \qquad (38)$$

and $\mathscr{F}(u)$ denotes Dawson's integral, given by

$$\mathscr{F}(u) = \exp(-u^2)\int_0^u \exp(\alpha^2)\,\mathrm{d}\alpha, \qquad (39)$$

Dawson's integral may be computed effectively, see Newman (1987). Applying (36) and (37) we obtain

$$\begin{aligned}
\frac{\partial\phi_{\pm L}(\pm L, y, t)}{\partial t} &= \pm\frac{\dot{Q}(\pm L, t_k)}{\pi h}\int_{-h}^0 \ln\frac{|y-y'|}{|y+y'|}\mathrm{d}y' \\
&\mp \frac{4g(\Delta t)^2}{\pi h}\sum_{m=0}^{k-1}(k-m)\,\dot{Q}(\pm L, t_m)\left\{\mathscr{F}_2\left[\frac{t_k-t_m}{2}(g/|y-h|)^{\frac{1}{2}}\right] - \mathscr{F}_2\left(\frac{t_k-t_m}{2}(g/|y|)^{\frac{1}{2}}\right)\right\}, \qquad (40)
\end{aligned}$$

where $\dot{Q} = \mathrm{d}Q/\mathrm{d}t$.

Convergence of the numerical scheme is achieved by increasing the value of N and decreasing the time step Δt. No smoothing is applied. We find that the simulations have converged for $N = O(100)$ and $\Delta t(g/h)^{\frac{1}{2}} = O(0.1)$, giving the integrated quantities with at least three significant digits, except close to the patching boundary in the most nonlinear examples (corresponding to the spilling limit) where a small (unimportant) reflection appears (see figures 8 and 10).

4.5. *The far-field waves*

The superharmonics introduce volume fluxes at the gaps which for $t \to \infty$ behave as

$$Q(\pm L, t) = \mathrm{Re}\sum_{n\geqslant 1} Q_{\pm L}^{(n)} \exp(\mathrm{i}n\omega)\,t + O(1/t). \qquad (41)$$

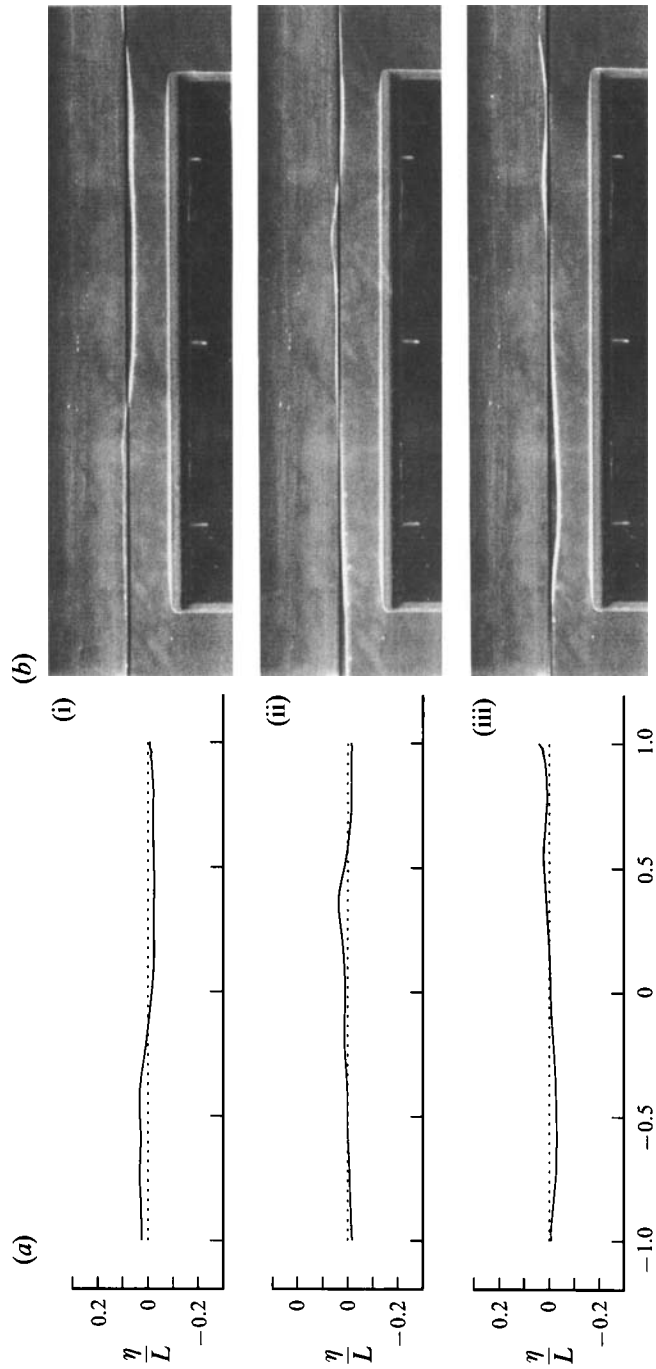

FIGURE 6. Deformation of the waves at the shelf in a natural scale; $h = 37.5$ mm, $2L = 500$ mm, $\omega = 2\pi \times 0.95$ Hz ($\omega^2 h/g = 0.136$), $a = 5.1$ mm ($a/h = 0.136$). (*a*) Numerical simulations ($N = 100$, $\Delta t(g/h)^{\frac{1}{2}} = 0.1$), (i–iii) Surface elevation at time intervals $P(g/h)^{\frac{1}{2}} = 5.7$ (corresponding to $P = 0.35$ s). (*b*) Time-lapse photographs of the surface elevation, (i–iii) at time intervals $P = 0.35$ s.

The velocity potentials $\phi_{\pm L}$ become accordingly

$$\phi_{\pm L}(x,y,t) = \pm \mathrm{Re}\left\{ \sum_{n\geqslant 1} \frac{2}{h} Q_{\pm L}^{(n)} \exp(\mathrm{i}n\omega t) \int_{-h}^{0} G^{(n)}(x,y,\pm L,y')\,\mathrm{d}y' \right\} + O(1/t), \quad (42)$$

where $G^{(n)}$ denotes the Green function due to a point source with unit strength, oscillating with frequency $n\omega$. For $x \to \pm\infty$ we have

$$G^{(n)} = \mathrm{i}\exp[K_n(y+y' \mp \mathrm{i}(x \mp L))], \quad x \to \pm\infty, \quad (43)$$

where the wavenumber for the nth mode is given by $K_n = n^2\omega^2/g = n^2K$. The free-surface elevation far away from the shelf then is given by

$$\eta(x,t) = \mathrm{Re} \sum_{n\geqslant 1} A_{+}^{(n)} \exp \mathrm{i}(n\omega t - K_n(x-L)), \quad x \to \infty, \quad (44)$$

$$\eta(x,t) = \mathrm{Re}\{a\exp \mathrm{i}(\omega t - K(x+L)) + \sum_{n\geqslant 1} A_{-}^{(n)} \exp \mathrm{i}(n\omega t + K_n(x+L))\}, \quad x \to -\infty, \quad (45)$$

where

$$A_{+}^{(n)} = (2Q_L^{(n)}/n\omega h)(1-\exp(-K_n h)), \quad (46)$$

$$A_{-}^{(n)} = -(2Q_{-L}^{(n)}/n\omega h)(1-\exp(-K_n h)) + \delta_{n1}\, a, \quad (47)$$

and δ_{n1} denotes the Dirac delta function. Thus, the amplitude of the nth-harmonic wave is related directly to the nth-harmonic component of the volume flux at the gap.

4.6. *Numerical results; comparison with experiments*

From (46) and (47) we obtain respectively the far-field amplitudes $a_{+}^{(n)}$ and $a_{-}^{(n)}$ for the same parameters as in the experiments. The theoretical predictions of $a_{+}^{(n)}$, $n = 1, 2, 3$, as functions of the incoming wave amplitude are shown in figure 4 for $\omega^2 h/g = 0.136$ and $h/2L = 0.075$, and in figure 5 for $\omega^2 h/g = 0.22$ and $h/2L = 0.1$, in addition to the experimental results. The theory shows overall a good agreement with the experiments even close to the spilling limit. The agreement is very good for small and moderate a. We remark that the theory predicts the strongly nonlinear behaviour of $a_{+}^{(2)}/a$ and $a_{+}^{(3)}/a$ particularly well in the example with the longest incoming wave and smallest h (figure 4).

The superharmonic wave amplitudes at the weather side, $a_{-}^{(n)}$, $n = 2, 3, \ldots$, obtained by (47), are always very small, in agreement with the experiments. This is because the volume flux $Q(-L,t)$ at the left end of the shelf shows, practically speaking, no signs of superharmonic oscillations, even for larger incoming wave amplitudes.

To more closely examine the deformation of the incoming waves we show in figures 6 and 7 numerical simulations in a natural scale and photographs of the surface elevation at the shelf for successive time instants. In figure 6 the amplitude is $a =$ 5.1 mm which corresponds to the spilling limit in the experiments. In figure 7 the amplitude is 7.5 mm which is slightly less than the spilling limit at 8 mm. The agreement between the theory and experiments is striking. The figures exhibit how the long incoming wave with one well-defined crest steepens at the left end of the shelf (figures 6(i), 7(i)). When the wave has moved to the right end, however, we clearly observe that higher-harmonic wave components are superposed on the longer wave (figures 6(ii, iii), 7(ii)), introducing superharmonic oscillations in $Q(L,t)$ with corresponding strength.

The deformation of the waves as a function of the incoming wave amplitude is

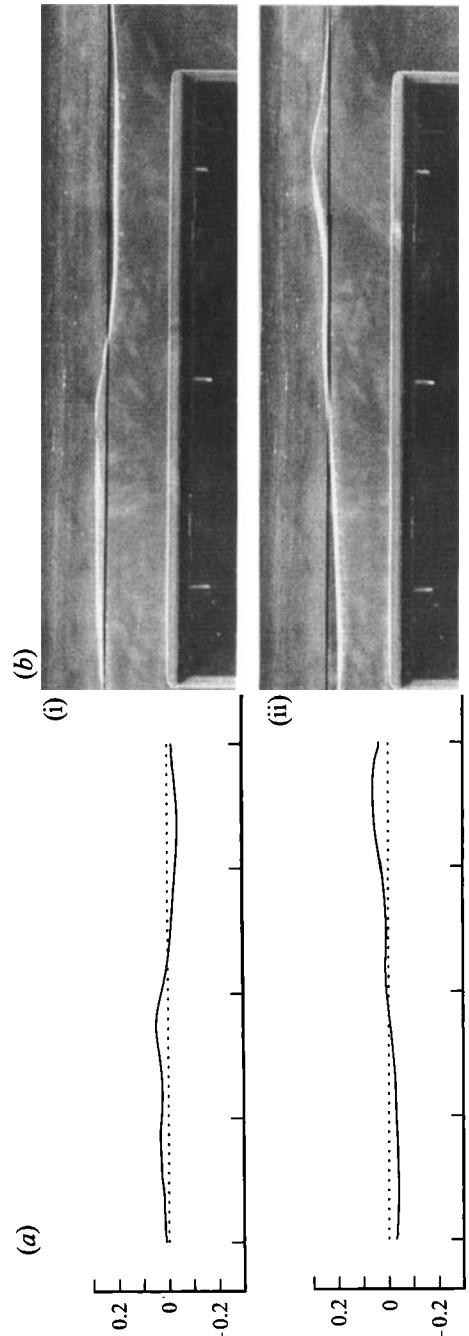

FIGURE 7. Deformation of the waves at the shelf in a natural scale; $h = 50$ mm, $2L = 500$ mm, $\omega = 2\pi \times 1.05$ Hz ($\omega^2 h/g = 0.22$), $a = 7.5$ mm ($a/h = 0.15$). (*a*) Numerical simulations ($N = 100$, $\Delta t(g/h)^{\frac{1}{2}} = 0.1$), (i, ii) Surface elevation at time intervals $P(g/h)^{\frac{1}{2}} = 4.9$ (corresponding to $P = 0.35$ s). (*b*) Time-lapse photographs of the surface elevation, (i, ii) at time intervals $P = 0.35$ s.

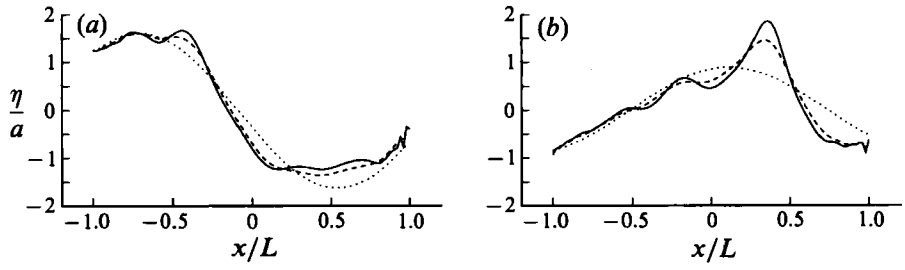

FIGURE 8. Surface elevation above the shelf; $h/2L = 0.075$, $\omega^2 h/g = 0.136$. Numerical simulations with $N = 100$, $\Delta t(g/h)^{\frac{1}{2}} = 0.1$: ——, $a/h = 0.136$; – – –, $a/h = 0.1$; ·····, $a/h = 0$. (*a*) Same time instant as in figure 6(i). (*b*) Same time instant as in figure 6(ii).

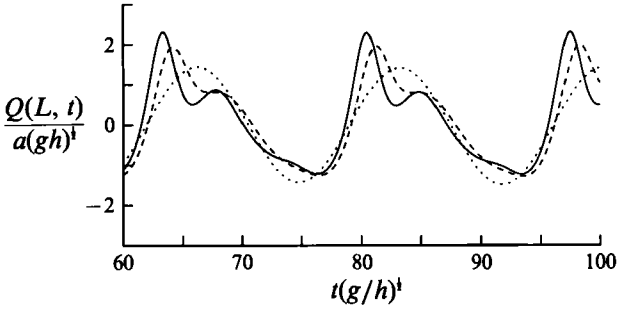

FIGURE 9. Volume flux $Q(L,t)$; $h/2L = 0.075$, $\omega^2 h/g = 0.136$. Numerical simulations with $N = 100$, $\Delta t(g/h)^{\frac{1}{2}} = 0.1$: ——, $a/h = 0.136$; – – –, $a/h = 0.1$; ·····, $a/h = 0$.

exhibited in figure 8(*a*, *b*) for the free-surface elevation and in figure 9 for the volume flux at $x = L$. We note the strong presence of the second- and third-harmonic components in the free-surface elevation and the volume flux $Q(L,t)$. The numerical simulations show that there are significant interactions up to the fifth time-harmonic oscillation for the largest incoming wave amplitude.

We have also done some numerical simulations by neglecting the dispersion in the shallow region. The Boussinesq equations are then reduced to the nonlinear Airy equations. For small values of a/h, when the generation of the shorter waves is weaker and the effect of the dispersion is correspondingly small, the Airy equations and Boussinesq equations give coinciding results. For larger a/h the Airy equations are found to predict unrealistically steep wave profiles in the shallow region, introducing reflection of shorter waves at $x = L$.

4.7. *The mean energy flux*

As a check of the computations we invoke the mean energy flux at a vertical control surface extending from the bottom of the fluid layer to the free surface, which at a location x is given by

$$R_x = \overline{\int_{\text{bottom}}^{\eta} (p + \tfrac{1}{2}\rho|\boldsymbol{v}|^2 + \rho g y)\, u \, \mathrm{d}y}. \tag{48}$$

Here $\boldsymbol{v}$ denotes the velocity vector in the fluid and a bar the time average. In the shallow region we obtain

$$R_x = \overline{\rho u(h+\eta)\left(g\eta + \tfrac{1}{2}u^2 - \tfrac{1}{3}(h+\eta)^2 \frac{\partial^2 u}{\partial t\, \partial x}\right)}. \tag{49}$$

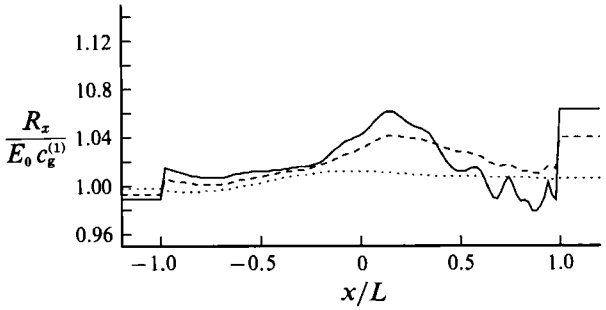

FIGURE 10. Time-averaged energy flux *vs.* horizontal coordinate; $h/2L = 0.075$, $\omega^2 h/g = 0.136$, $N = 100$, $\Delta t(g/h)^{\frac{1}{2}} = 0.1$: ——, $a/h = 0.136$; – – –, $a/h = 0.1$; ·····, $a/h = 0$.

For $t \to \infty$ the mean energy flux at $x = -\infty$ is given by

$$R_{-\infty} = E_0 c_g^{(1)} - \sum_{n \geqslant 1} E_-^{(n)} c_g^{(n)}, \tag{50}$$

and at $x = \infty$ by

$$R_\infty = \sum_{n \geqslant 1} E_+^{(n)} c_g^{(n)}, \tag{51}$$

where $E_0 = \frac{1}{2}\rho g a^2$, $E_-^{(n)} = \frac{1}{2}\rho g |A_-^{(n)}|^2$ and $E_+^{(n)} = \frac{1}{2}\rho g |A_+^{(n)}|^2$ denote the mean energy densities of the incoming, reflected and transmitted waves, respectively; $c_g^{(n)} = \frac{1}{2}g/n\omega$, $n = 1, 2, \ldots$, denote the corresponding group velocities of the incoming and scattered waves.

The value of $R_{-\infty}$ gives R_x for $x \leqslant -L^-$, and R_∞ gives, correspondingly, R_x for $x \geqslant L^+$. In figure 10 we show R_x as function of the incoming wave amplitude and horizontal coordinate. The figure illustrates that the numerical scheme (31)–(32) introduces a small variation in the energy flux along the horizontal coordinate, which in the linear case is about 1%. There is also a net increase in $R_x/E_0 c_g^{(1)}$ across the shelf that is proportional to the incoming wave amplitude when this is finite. This net increase is obviously introduced due to the patching at the gaps between the nonlinear and linear flows and indicates the error in the model due to the patching. We observe that the variation in R_x is smooth, except in the most nonlinear case, which corresponds to the spilling limit in the experiments. Then small rapid variations are observed close to $x = L$. These variations, with counterparts in figure 8(*a*, *b*), illustrate the numerical reflection introduced by the patching between the linear and nonlinear flow regimes. The numerical reflection is, however, very small and vanishes for small and moderate a/h.

5. Conclusions

We have experimentally and theoretically studied incoming deep water waves with small wave slope propagating over a slightly submerged circular cylinder or a rectangular shelf. The wavelength is much greater than the local water depth above the obstacle. Nonlinear free-surface effects at the obstacle introduce asymmetry and skewness to the initially symmetric wave profile, and generate a hierarchy of shorter superharmonic free waves propagating away from the obstacle, superposed upon the transmitted and reflected waves with wavelength equal to the incoming wavelength. The superharmonic waves may attain prominent amplitudes at the obstacle's lee side. This is not true at the weather side of the obstacle where the superharmonic waves are very small. The measurements indicate that there are no first- and higher-

harmonic reflected waves by the circular cylinder. The generation of the higher-harmonic waves at the lee side becomes more and more powerful with increasing incoming wave amplitude up to when breaking occurs at the obstacle. At the breaking limit the amplitudes of the second- and third-harmonic waves attain maximal values compared to the incoming wave amplitude, and are in some examples found to be of the same order of magnitude as the first-harmonic transmitted waves. We find that up to about 25% of the incoming energy flux may be transferred to the super-harmonic waves.

The theoretical model developed for the shelf geometry accounts for nonlinearity by the Boussinesq equations in the shallow region above the shelf, with patching at the edges to linearized potential theory applied in the deep water. The theoretical and experimental results for the local flow at the shelf and in the far-field show good agreement for non-breaking waves. The theoretical model emphasizes that both nonlinearity and dispersion are important at the obstacle, while dispersion is the dominating effect for the flow far away. The patching procedure applied between the linear and nonlinear flows is very efficient in the present examples.

The author acknowledges Dr Geir Pedersen for providing the Boussinesq equation solver, and the assistance by Arve Kvalheim, Øyvind Strand and Svein Vesterby with the experimental set up. Preliminary results were presented at the 3rd and 4th Intl Workshops on Water Waves and Floating Bodies held respectively at Woods Hole, Massachusetts, USA, 1988, and Øystese, Norway, 1989. The theoretical part of this research was initiated while the author was visiting at Dept. of Ocean Engineering, MIT, USA, 1987–88, kindly sponsored by Jansons Legat, the Royal Norwegian Council for Science and the Humanities (NAVF) and the Scandinavian American Association.

REFERENCES

CHAPLIN, J. R. 1984 Nonlinear forces on a horizontal cylinder beneath waves. *J. Fluid Mech.* **147**, 449–464.

COINTE, R. 1989 Nonlinear simulation of transient free surface flows. *5th Intl Conf. on Numerical Ship Hydrodynamics, Hiroshima, September.*

DEAN, W. R. 1948 On the reflexion of surface waves by a circular cylinder. *Proc. Camb. Phil. Soc.* **40**, 19.

FRIIS, A. 1990 Second order diffraction forces on a submerged body by second order Green function method. *Abstr. 5th Intl Workshop on Water Waves and Floating Bodies*, Manchester, UK (ed. P. A. Martin).

FRIIS, A., GRUE, J. & PALM, E. 1991 Application of Fourier transform to the second order 2D wave diffraction problem. In *M. P. Tulin's Festschrift: Mathematical Approaches in Hydrodynamics* (ed. T. Miloh). SIAM.

GRUE, J. & GRANLUND, K. 1988 Impact of nonlinearity upon waves travelling over a submerged cylinder. *Abstr. 3rd Intl Workshop on Water Waves and Floating Bodies, Woods Hole, Mass.* (ed. F. T. Korsmeyer).

GRUE, J. & PALM, E. 1985 Wave radiation and wave diffraction from a submerged body in a uniform current. *J. Fluid Mech.* **151**, 257–278.

LEE, C. M. 1968 The second order theory of heaving cylinders in a free surface. *J. Ship Res.* **12**, 313–327.

LONGUET-HIGGINS, M. S. 1977 The mean forces exerted by waves on floating or submerged bodies with applications to sand bars and wave power machines. *Proc. R. Soc. Lond.* A **352**, 463–480.

MCIVER, M. & MCIVER, P. 1990 Second-order wave diffraction by a submerged circular cylinder. *J. Fluid Mech.* **219**, 519–529.

MEI, C. C. 1989 *The Applied Dynamics of Ocean Surface Waves*, 2nd edn. World Scientific.

MILES, J. W. 1967 Surface-wave scattering matrix for a shelf. *J. Fluid Mech.* **28**, 755–767.

NEWMAN, J. N. 1965 Reflection and transmission of water waves past long obstacles. *J. Fluid Mech.* **23**, 399–415.

NEWMAN, J. N. 1987 Evaluation of the wave resistance Green Function: Part 2 – The single integral on the centerplane. *J. Ship Res.* **31**, 145–150.

NEWMAN, J. N., SORTLAND, B. & VINJE, T. 1984 Added mass and damping of rectangular bodies close to the free surface. *J. Ship Res.* **28**, 219–225.

PALM, E. 1991 Nonlinear wave reflection from a submerged cylinder. *J. Fluid Mech.* **233**, 49–63.

PEDERSEN, G. K. 1991 Finite difference representations of nonlinear waves. *Intl J. Numer. Meth. Fluids* **13**, 671–690.

VADA, T. 1987 A numerical solution of the second-order wave diffraction problem for a submerged cylinder of arbitrary shape. *J. Fluid Mech.* **174**, 23–37.

WEHAUSEN, J. V. & LAITONE, E. V. 1960 Surface waves. In *Handbuch der Physik IX*. Springer.

WILLIAMS, J. A. 1964 A nonlinear problem in surface water waves. Ph.D. thesis, Dept. of Naval Arch. & Offsh. Engng, University of California, Berkeley.

YEUNG, R. W. 1982 Transient heaving motion of floating cylinders. *J. Engng. Maths* **16**, 97–119.